nature energy

ARTICLES

https://doi.org/10.1038/s41560-022-01018-5

OPEN

Light-induced activation of boron doping in hydrogenated amorphous silicon for over 25% efficiency silicon solar cells

Wenzhu Liu[1,12] ✉, Jianhua Shi[1,2,12], Liping Zhang[1,2,12], Anjun Han[1,2,12], Shenglei Huang[1], Xiaodong Li[1], Jun Peng[3], Yuhao Yang[1], Yajun Gao[4], Jian Yu[5], Kai Jiang[1], Xinbo Yang[6], Zhenfei Li[1], Wenjie Zhao[1], Junlin Du[1,2], Xin Song[7], Jun Yin[4], Jie Wang[8], Youlin Yu[1], Qiang Shi[1], Zhixin Ma[1], Haichuan Zhang[2,9], Jiajia Ling[10], Lujia Xu[4], Jingxuan Kang[4], Fuzong Xu[4], Jiang Liu[4], Hanyuan Liu[2,9], Yi Xie[2,9], Fanying Meng[1,2], Stefaan De Wolf[4], Frédéric Laquai[4], Zengfeng Di[11] and Zhengxin Liu[1,2,9] ✉

Recent achievements in amorphous/crystalline silicon heterojunction (SHJ) solar cells and perovskite/SHJ tandem solar cells place hydrogenated amorphous silicon (a-Si:H) at the forefront of photovoltaics. Due to the extremely low effective doping efficiency of trivalent boron in amorphous tetravalent silicon, light harvesting of aforementioned devices is limited by their fill factors (FFs), a direct metric of the charge carrier transport. It is challenging but crucial to develop highly conductive doped a-Si:H with minimal FF losses. Here we report that light soaking can efficiently boost the dark conductance of boron-doped a-Si:H thin films. Light induces diffusion and hopping of weakly bound hydrogen atoms, which activates boron doping. The effect is reversible and the dark conductivity decreases over time when the solar cell is no longer illuminated. By implementing this effect to SHJ solar cells, we achieved a certified total-area power conversion efficiency of 25.18% with a FF of 85.42% on a 244.63 cm² wafer.

Hydrogenated amorphous silicon (a-Si:H) is a technologically important semiconductor for transistors, batteries and solar cells[1–4]. It has a long history of use in photovoltaic applications as it offers a low defect density and tunable conduction type[5–7]. These optoelectronic advantages strongly rely on configurations of hydrogen and silicon in the three-dimensional space (described by the radial distribution function[8]) and thus precise control of its microscopic structure[9–11] is a critical factor towards achieving good devices. As boron is a trivalent element, it is challenging to establish four-coordinated B–Si_4 compounds in the disordered a-Si:H matrix; reported approaches, which are focused on eliminating invalid Si_x–B–H_y doping configurations (Supplementary Fig. 1), include optimizing the B_2H_6 flow rate and post-deposition annealing. However, a lack of understanding of the complicated conduction mechanism of boron-doped a-Si:H (p-a-Si:H) has obstructed the full potential of relevant optoelectronic devices.

We find that light soaking is a fast means to improving dark conductance (σ_{dark}) of p-a-Si:H thin films. Our results indicate that a portion of hydrogen atoms is captured by tetravalent-coordinated boron atoms in the silicon network to form weak B–H–Si components, which diminishes the efficient B–Si_4 doping. We demonstrate that the key function of light soaking is to promote the diffusion and hopping of these weakly bound hydrogen atoms, so that efficient B–Si_4 doping is activated. As a consequence of the improved field passivation and conductivity of p-a-Si:H, we achieve a high power conversion efficiency (PCE) of 25.18% with an open-circuit voltage (V_{oc}) and fill factor (FF) of 749 mV and 85.42%, respectively, on a 244.63 cm² amorphous/crystalline silicon heterojunction (SHJ) solar cell. Moreover, our 60-cell modules exhibit a robust operating stability that successfully passes IEC 60068-2-78 (damp-heat degradation at 85 °C and 85% relative humidity, DH85) and IEC 61215-2:2016 (thermal cycle degradation between −40 °C and 85 °C with applied current at 100% I_{mpp} (current at the maximum power point) at the rising edge of temperature) even after threefold-time-long aging standards.

Observation of light-induced dark conductivity increase

Since 1977, light soaking of micrometre-thick a-Si:H films has been widely studied in the research field of a-Si:H thin-film solar cells, but only a small number of works pay attention to its effect on 'thin' a-Si:H films, particularly in the research field of SHJ solar cells[12,13]. Although a few researchers report that light soaking improves the FF of SHJ solar cells by a magnitude of ~0.7%$_{abs}$ (ref. [14]), the fundamental underlying mechanisms are still unclear, which attracts broad interest in the research fields of optoelectronics. We use in situ methods to monitor the time-dependent changes

[1]Research Center for New Energy Technology, Shanghai Institute of Microsystem and Information Technology (SIMIT), Chinese Academy of Sciences (CAS), Shanghai, China. [2]Zhongwei New Energy (Chengdu) Company, Sichuan, China. [3]School of Engineering, The Australian National University, Canberra, Australia. [4]King Abdullah University of Science and Technology (KAUST), KAUST Solar Center (KSC), Thuwal, Saudi Arabia. [5]Institute of Photovoltaics, Southwest Petroleum University, Chengdu, China. [6]College of Energy, Soochow Institute for Energy and Materials Innovations (SIEMIS), Soochow University, Suzhou, China. [7]School of Materials Science and Engineering, Jiangsu Collaborative Innovation Center of Photovoltaic Science and Engineering, Changzhou University, Changzhou, China. [8]College of Minerals Processing and Bioengineering, Central South University, Changsha, China. [9]Tongwei Solar Company, Sichuan, China. [10]UISEE Technologies (Shanghai) Company, Shanghai, China. [11]State Key Laboratory of Functional Materials for Informatics, Shanghai Institute of Microsystem and Information Technology, Chinese Academy of Sciences, Shanghai, China. [12]These authors contributed equally: Wenzhu Liu, Jianhua Shi, Liping Zhang, Anjun Han. ✉e-mail: wenzhu.liu@mail.sim.ac.cn; z.x.liu@mail.sim.ac.cn

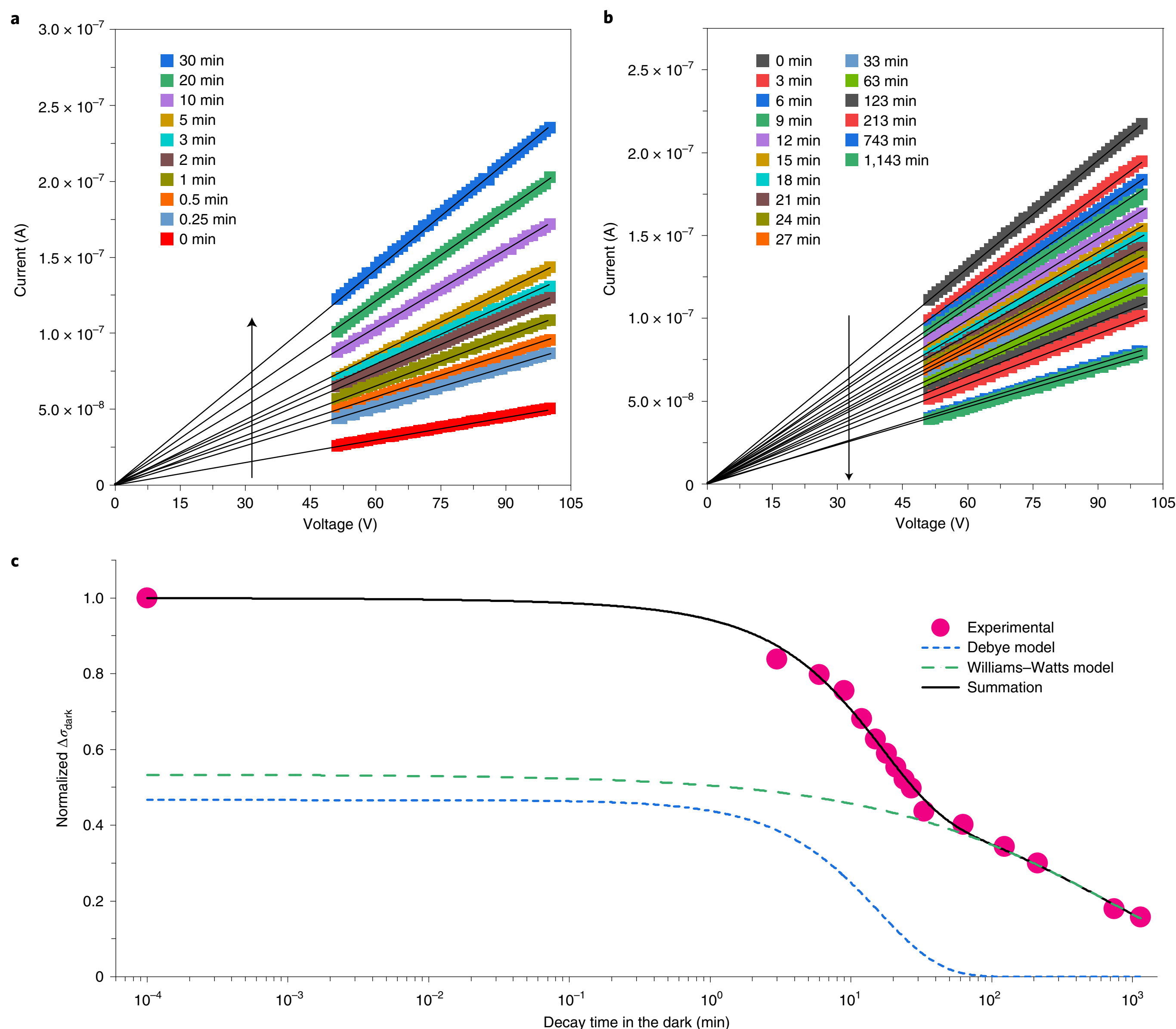

Fig. 1 | Observation of the light-induced dark conductivity increase. a, Dark current–voltage evolution of p-a-Si:H thin film as a function of light soaking time under 1 sun illumination (100 mW cm^{-2} at 25 °C). The curves are linear fits through the origin (0, 0). **b**, Dark current–voltage evolution of light-soaked p-a-Si:H thin film as a function of time in the dark following light soaking. The curves were fitted using equation (1), where the derived results are summarized in Supplementary Table 1. **c**, Normalized decay of $\Delta\sigma_{dark}$ fits to a combination of Debye model and Williams–Watts model.

of p-a-Si:H thin films during illuminations. The films are deposited on quartz glasses, followed by evaporating silver strips to form the transfer-length-method structures. The in situ current–voltage data (Fig. 1a) show that σ_{dark} of the p-a-Si:H thin film steadily increases during 1 sun illumination, reaching $\sigma_{dark}/\sigma_{dark0} \approx 4.71$ (σ_{dark0} is dark conductance before light soaking) after 30 min. This phenomenon is strikingly in contrast to the light-induced degradation of σ_{dark} observed in thick intrinsic, p- and n-type a-Si:H films[15–17]. It supports the perspective that accumulated stress in thick films plays an important role in the Staebler–Wronski effect[18], as the maximum stress is roughly proportional to the film thickness. This indicates the effect of light soaking exhibits a scaling behaviour, where the Staebler–Wronski effect gradually transitions to a different effect as the thickness declines. After turning off the illumination, σ_{dark} gradually decays (close) to its initial value after more than 1,000 min (Fig. 1b). Such a decay behaviour fits well to a combination of the Debye and Williams–Watts models (Fig. 1c),

$$\Delta\sigma_{dark}(t) = \Delta\sigma_D \exp\left[-(t/\tau_D)^{\beta_D}\right] + \Delta\sigma_{WW} \exp\left[-(t/\tau_{WW})^{\beta_{WW}}\right], \quad (1)$$

The terms $\Delta\sigma_D$, $\Delta\sigma_{WW}$ and τ_D, τ_{WW} are constant coefficients and characteristic time constants of the Debye and Williams–Watts models, respectively. The term t is the decay time in the dark. Detailed parameters are summarized in Supplementary Table 1. The Debye model with $\beta_D = 1$ describes free diffusion, whereas the Williams–Watts model with $0 < \beta_{WW} < 1$ describes a continuous-time random walk composed of alternating steps and pauses[19]. Examples of the Williams–Watts model include the spin-correlation in Cu–Mn and

Ag–Mn, spin glass transition in $BaFe_{12}O_{19}$, dielectric relaxation in $K_{0.3}MoO_3$, spin-lattice relaxation in κ-$(ET)_2Cu[N(CN)_2]Br$ (here ET represents bis(ethylenedithio)tetrathiafulvalene), specific heat in Fe_xZr_{1-x} and hydrogen relaxation in a-Si (refs. [20–25]). The good fitting in Fig. 1c suggests an effect that is different to the Staebler–Wronski effect and mediated by two independent mechanisms that control the fast Debye relaxation and the slow Williams–Watts relaxation, respectively.

Mechanism underlying the light-induced changes

To determine the implicit mechanisms of aforementioned Debye and Williams–Watts relaxation, we investigate the hydrogen distributions in p-a-Si:H thin films by time-of-flight secondary ion mass spectrometry (TOF-SIMS). The H^- spectra (Fig. 2a) show that 30 min annealing at 180 °C only slightly changes the hydrogen content in intrinsic a-Si:H (i-a-Si:H), by contrast, the same annealing process expels at least ~21.3% of the hydrogen content from p-a-Si:H. As shown in Supplementary Fig. 2, TOF-SIMS spectra also reveal that room-temperature oxidation of an i/p-a-Si:H stack hardly changes the hydrogen content in the i-a-Si:H film, however, the same oxidation process expels ~17.1% of the hydrogen content in p-a-Si:H from the inside to the surface. Based on these findings, we conclude that the boron doping plays a crucial part in the formation of metastable hydrogen configurations in p-a-Si:H.

We next consider the migration barriers of hydrogen atoms to understand the possible binding configurations of aforementioned metastable hydrogen. Structural relaxations observed displacement of four-coordinated silicon atoms by boron atoms shorten the bonds from ~2.35 Å to ~2.07 Å (Supplementary Fig. 3), well consistent with the results of Pandey and colleagues[26]. Further simulations demonstrate that these $B{-}Si_4$ sites have a large probability of attracting hydrogen atoms to form metastable B−H−Si configurations when diffusive hydrogen atoms pass by (Supplementary Fig. 4), which is in agreement with the nuclear magnetic resonance signal[27] and relevant simulations[26,28]. As a consequence, conductance of p-a-Si:H is expected to decline due to reduction in the quantity of $B{-}Si_4$ (ref. [26]). Transition-state surveys (Fig. 2b,c) prove that the hopping barriers of hydrogen from B−H−Si and Si−H−Si to adjacent Si−H−Si are 0.88 ± 0.16 eV (A to B in Fig. 2b) and 0.64 ± 0.16 eV (B to C in Fig. 2b), respectively; reversely, the hopping barriers of hydrogen from Si−H−Si to Si−H−Si and B−H−Si are 0.42 ± 0.12 eV (C to B in Fig. 2b) and 0.61 ± 0.15 eV (B to A in Fig. 2b), respectively. Consideration of the barriers (the energy difference between A and C is ~0.46 eV) in Fig. 2c and the binding energy of hydrogen in Si−H−Si (0.5−1.05 eV) concludes[29,30] that the binding energy of trapped hydrogen in B−H−Si is about 0.96−1.51 eV, noticeably lower than those (>3 eV) of Si−H bonds, which accounts for why much more metastable hydrogen configurations exist in p-a-Si:H than in i-a-Si:H (inferred from Fig. 2a). When light soaking under 1 sun illumination provides photons with energy over ~0.88 eV, huge amounts of $Si_3{-}B{-}H$ should be converted to $B{-}Si_4$ via the hydrogen hopping mechanism (or the tunnelling mechanism[31] at temperatures below 60 K) illustrated in Fig. 2b, resulting in improvement of σ_{dark} as has been confirmed in Fig. 1a. The microscopic migrations in Fig. 2b are consistent with the light-induced formation of Si−H−Si configurations[32].

The mechanistic understanding is also evident in optoelectronic analysis. We prepared symmetric structures of p-a-Si:H/i-a-Si:H/n-c-Si/i-a-Si:H/p-a-Si:H (here n-c-Si represents n-type c-Si) and i-a-Si:H/n-c-Si/i-a-Si:H, whose injection-dependent effective minority carrier lifetimes (τ_{eff}) were measured before and after 2 h light soaking under 1 sun illumination, as well as that after 15 min annealing at 180 °C. The right graph in Fig. 2d shows that the τ_{eff} of p-a-Si:H/i-a-Si:H/n-c-Si/i-a-Si:H/p-a-Si:H increased substantially after light soaking and then returned to initial values after the annealing. The recombination rate at the a-Si:H/c-Si interface satisfies a closed-form expression in case of high illumination, which can be fitted by the model of Olibet and colleagues[30]; by modelling the τ_{eff} at injection $>1.0 \times 10^{15}$ cm^{-3}, we determined that light soaking increased (decreased) the surface charge density Q_s (the interface dangling-bond density N_s) from 3.0×10^{10} cm^{-2} (2.1×10^{9} cm^{-2}) to 3.8×10^{10} cm^{-2} (1.4×10^{9} cm^{-2}), and then annealing decreased (increased) the Q_s (N_s) back to 3.0×10^{10} cm^{-2} (2.0×10^{9} cm^{-2}). As a control, the left graph in Fig. 2d shows that the τ_{eff} of i-a-Si:H/n-c-Si/i-a-Si:H almost remained constant after either light soaking or annealing, which demonstrates that the variation in τ_{eff} in the right graph must originate from p-a-Si:H. According to Sinton and co-workers[33], pseudo FFs (PFFs) of silicon solar cells take into account the effect of chemical passivation. We probed the PFF of the device Ag/IWO/p-a-Si:H/i-a-Si:H/n-c-Si/i-a-Si:H/n-a-Si:H/IWO/Ag (where IWO is tungsten-doped indium oxide) before and after 2 h light soaking under 1 sun illumination, as well as that after 15 min annealing at 180 °C. The inset of Fig. 2d finds that the PFF maintains a PFF of ~86.4% regardless of light soaking and annealing. This demonstrates that the decrease in N_s has a negligible impact on chemical passivation, probably due to the small order of magnitude of N_s itself. On the other hand, ultrafast and broadband transient absorption signals (Fig. 2e) indicate that light soaking increases the mobility of photon-generated carriers from 7.10×10^{-3} cm^2 V^{-1} s^{-1} to 1.81×10^{-2} cm^2 V^{-1} s^{-1} in p-a-Si:H. This probably results from less scattering of carrier transport in the p-a-Si:H network, thanks to the global decline of strain-induced gap states from B−H−Si configurations[26]. Consideration of these light-induced enhancements to σ_{dark}, Q_s and the carrier mobility leads to the conclusion that the light-induced dark conductivity increase stems from activation of boron doping via hydrogen movements. In this regard, we further ascribe the decay of σ_{dark} in Fig. 1c to the detrimental reconstruction of B−H−Si configurations, as the binding energy of hydrogen in B−H−Si is ~0.46 eV higher than that in Si−H−Si. In accordance, the fast Debye and slow Williams–Watts relaxations (Fig. 1c) are attributed to incorporation of fast diffusive hydrogen and slow hopping hydrogen into the B−Si bonds, respectively, forming invalid boron doping B−H−Si that has negative effects on the σ_{dark} as has been confirmed in Fig. 1b.

We next distinguish the weakly bound hydrogen atoms from the normal Si−H bonds in p-a-Si:H to strengthen the mechanism underlying the light-induced dark conductivity increase. Figure 3a illustrates the preparation of p-a-Si:H films for TOF-SIMS, Fourier-transform infrared spectroscopy (FTIR) and current–voltage characterizations. The capping of an IWO layer on the p-a-Si:H is to mimic the structure of SHJ solar cells, which may have an effect on the redistribution dynamics of hydrogen atoms during the annealing process. TOF-SIMS signals (Fig. 3b) find 2 h annealing at 180 °C reduced >20% of the hydrogen content in the p-a-Si:H film, whereas the content of silicon and boron (almost) remained unchanged. By contrast, Fig. 3c finds that all of the wagging, bending and stretching intensities of the normal Si−H bonds (almost) remain unchanged after the same annealing process. A comparison between the TOF-SIMS signals of hydrogen atoms and the FTIR spectra of Si−H bonds unambiguously demonstrates that relatively low-temperature (180 °C) annealing merely expels weakly bound hydrogen atoms from the p-a-Si:H film while the normal Si−H bonds are hardly affected. The light-induced enhancement of dark conductance of the p-a-Si:H film is plotted as a function of the annealing time at 180 °C in Fig. 3d, evidently, the $\sigma_{dark}/\sigma_{dark0}$ gradually declined to ~1 due to the exhaustion of weakly bound hydrogen atoms during the prolonged annealing. This definitely proves the light-induced dark conductivity increase and boron doping activation does stem from weakly bound hydrogen atoms rather than normal Si−H bonds in the p-a-Si:H.

According to Pandey and colleagues[26], there exist a host of possible configurations of weakly bound hydrogen atoms with respect

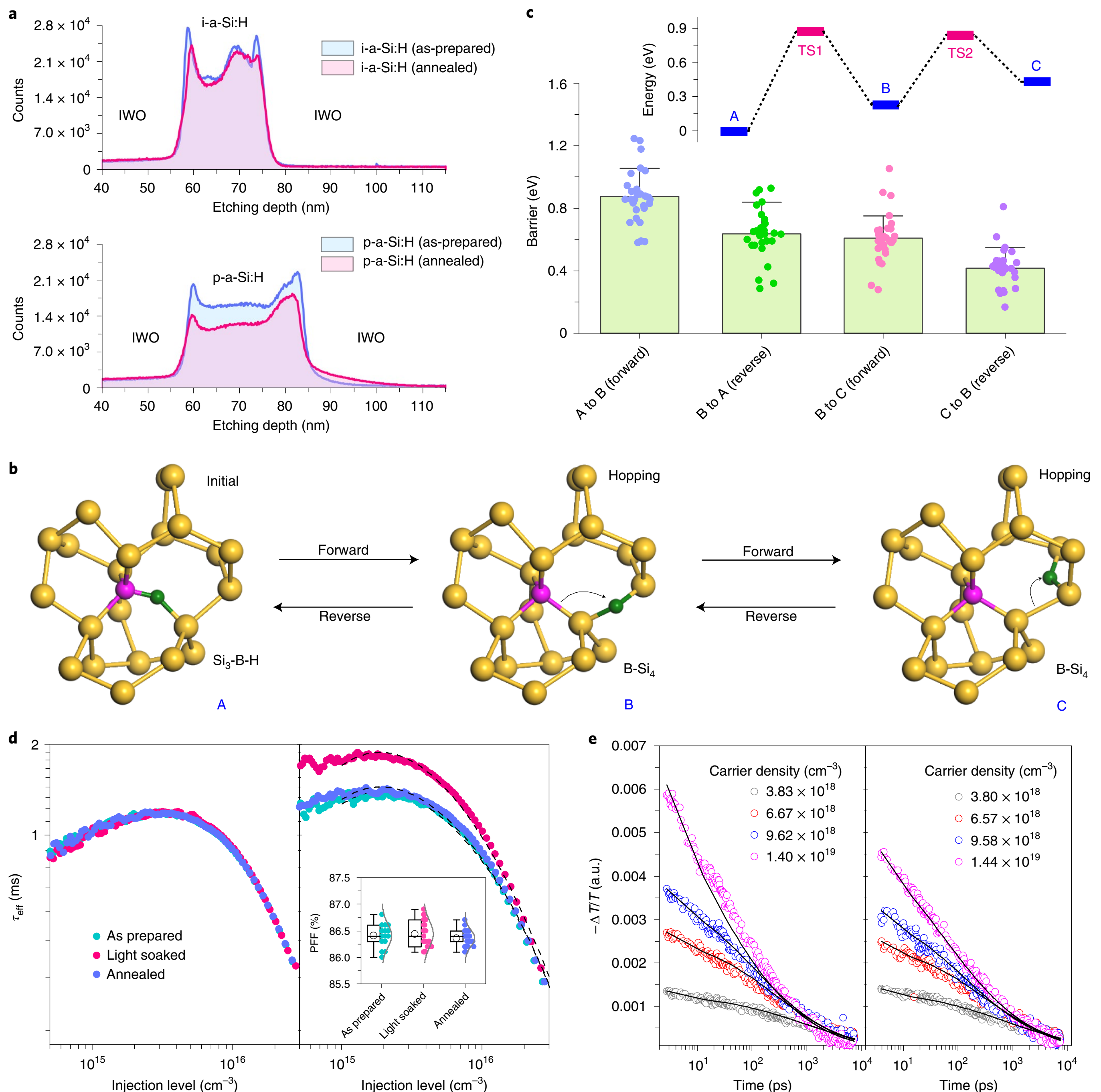

Fig. 2 | Mechanisms underlying the light-induced dark conductivity increase and boron doping activation. a, H^- profiles of i-a-Si:H and p-a-Si:H before and after 30 min annealing at 180 °C. Here IWO is a transparent conductive layer. **b**, Schematic hydrogen movements (indicated by black arrows) and relative binding configurations of the Bi–Si site, as inferred from the calculation of migration barriers. Yellow, silicon; magenta, boron; cyan, hydrogen. **c**, Energy barriers of hydrogen movements, each case has 30 data points calculated from different doping sites of boron atoms. The energies in the inset are in comparison to state A, as illustrated in **b**. The error bars are standard deviations. **d**, Injection-dependent τ_{eff} of p-a-Si:H/i-a-Si:H/n-c-Si/i-a-Si:H/p-a-Si:H (right) and i-a-Si:H/n-c-Si/i-a-Si:H (left) before and after 2 h light soaking under 1 sun illumination, as well as that after 15 min annealing at 180 °C (before which they are light soaked). τ_{eff} at injection level $>1.0\times10^{15}$ cm^{-3} is fitted using Olibet and colleagues' model[47]. The inset shows the PFF of complete SHJ solar cells before and after 2 h light soaking under 1 sun illumination, as well as that after 15 min annealing at 180 °C (before which they are light soaked). The top lines, bottom lines, lines in the box, circles and boxes represent maximum values, minimum values, median values, mean values and 25–75% distributions, respectively. **e**, Transient absorption signals of p-a-Si:H before (left) and after (right) 2 h light soaking under 1 sun illumination, the fitting is based on the one-dimensional recombination and diffusion model.

to boron atoms in the complicated p-a-Si:H network, such as weak hydrogen atoms nearby B–Si_4 doping, boron dimers and boron clusters and so on. By changing the flow rate of B_2H_6 during the film deposition, we fabricated four p-a-Si:H films on quartz glasses, their current–voltage characteristics are shown in Supplementary Fig. 5a. We find that dark conductance (Supplementary Fig. 5b) gradually

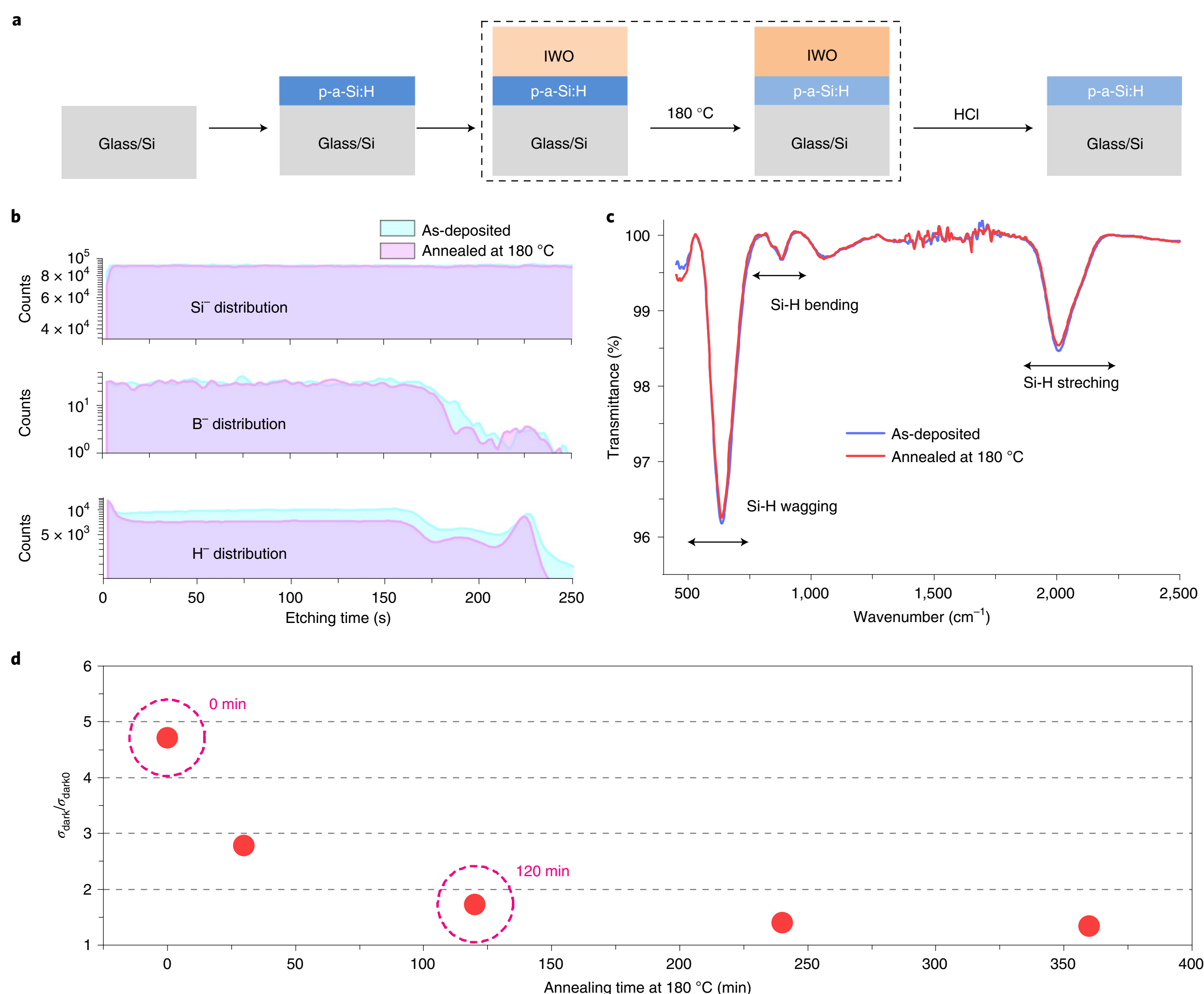

Fig. 3 | Direct evidence of weakly bound hydrogen atoms in p-a-Si:H and the impact on the light-induced dark conductivity increase. a, Sample preparation for measurements of TOF-SIMS, FTIR and current-voltage characteristics. After etching the IWO layer with an aqueous solution of HCl, p-a-Si:H on silicon is used for TOF-SIMS and FTIR characterizations, while p-a-Si:H on quartz glass is used for current-voltage characterization using the transfer-length-method structure. **b**,**c**, TOF-SIMS signals (**b**) and FTIR spectra (**c**) of p-a-Si:H after 0 min (blue) and 2 h annealing at 180 °C (red). **d**, Enhancement of dark conductance after 2 h light soaking under one sun illumination, plotted as a function of annealing time at 180 °C, where σ_{dark0} and σ_{dark} are dark conductance before and after the 2 h light soaking under 1 sun illumination. The two dashed circles correspond to p-a-Si:H films in **b** and **c**.

saturates when the flow rate of B_2H_6 exceeds ~45 sccm, which suggests that a huge amount of boron atoms are invalidly doped into p-a-Si:H, or do not make contribution to hole concentration. Furthermore, light-induced enhancement of dark conductance substantially decreases when the flow rate of B_2H_6 exceeds ~20 sccm (Supplementary Fig. 5c). Taking into account the possibility that boron dimers and clusters dominate only in case of high flow rates of B_2H_6 molecules, we conclude that the light-induced dark conductivity increase and boron doping activation mainly stem from the weak hydrogen atoms nearby the most important B–Si_4 doping sites, rather than those nearby boron-superabundant configurations, such as boron dimers and boron clusters and so on.

Application to high-efficient SHJ solar cells

Encouraged by the enhancement of σ_{dark} by light soaking, we attempt to develop the full potential of SHJ solar cells by this light-induced effect. Figure 4a showcases the device structure (where the thickness of the p-a-Si:H is ~15 nm; Supplementary Fig. 6) whose initial open-circuit voltage (V_{oc}), short-circuit current density (J_{sc}), FF and PCE are 744.30 ± 0.68 mV, 38.43 ± 0.07 mA cm^{-2}, 83.70 ± 0.22% and 23.94 ± 0.04% respectively, based on 316 continuous devices from our daily production line. Under 1 sun illumination, as expected, the FF of these cells undergoes a steady increase (standard cell in Fig. 4b). The slope of the current–voltage curve near the low-internal-field region (V_{oc} condition) serves as an indication of charge collection efficiency[35], as found in Supplementary Fig. 7, the light soaking continuously increases the slope near this low-internal-field region, indicating more efficient charge extraction due to enhancement of the net field across the depletion region. This strongly supports our perspective that the light soaking activates better boron doping. By contrast, we observe a noticeable drop in the gain of FF for devices annealed for 2 h at 180 °C (180 °C in Fig. 4b), attributed to its less metastable hydrogen configurations (inferred from Figs. 2a and 3b), which leads to less hydrogen movements in Fig. 2b. Intriguingly, we

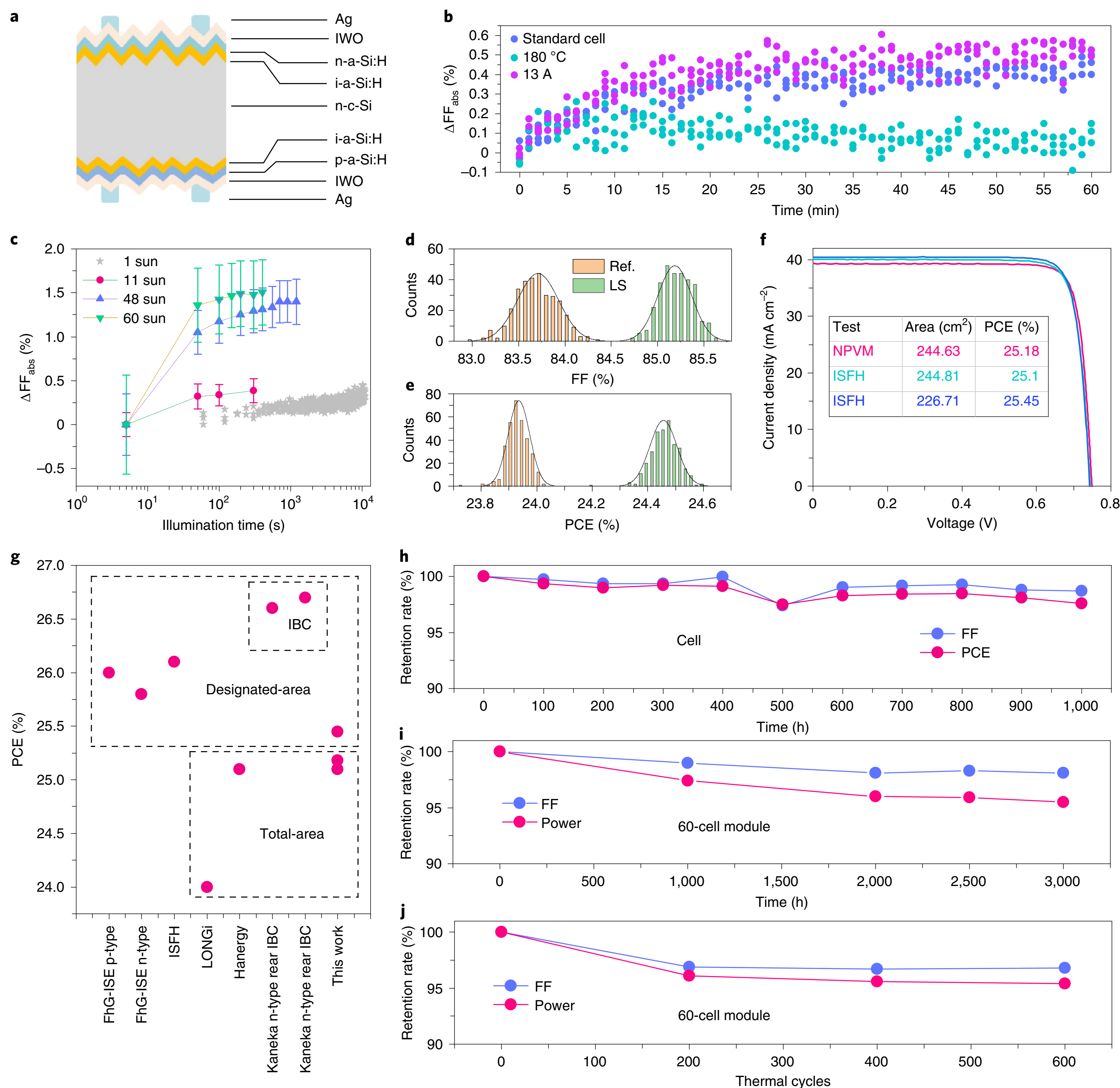

Fig. 4 | Improvement of SHJ solar cells by light-induced dark conductivity increase and boron doping activation. **a**, Device structure. **b**, FF evolution of as-prepared and annealed devices as a function of light soaking time under 1 sun illumination. Standard cell and 180 °C devices are as-prepared and annealed for 2 h at 180 °C, respectively. The FF evolution of 13 A devices is also shown. **c**, The FF evolution under different light intensities. Error bars on mean values are standard deviations from 20 devices. **d**,**e**, FF (**d**) and PCE (**e**) of 316 SHJ solar cells before (Ref.) and after (LS) 70 s of light soaking under 60 sun illumination. **f**, Current–voltage curves of SHJ solar cells tested by National Photovoltaic Industry Metrology and Testing Center (NPVM) and ISFH CalTeC (see Supplementary Data 1 for details). The ISFH results are tested in different modes, that is, one uses the total area (244.81 cm^2) whereas the other uses an aperture mask shadowing the cell edges. **g**, Comparison of PCEs with the best c-Si solar cells in the solar cell efficiency tables[34] and references therein. The total- and designated-area labels indicate testing using the total area and an aperture mask respectively. IBC indicates that electrodes are interdigitated-back-contacted. **h**, 1,000 h DH85 degradations of FF and PCE of six inch devices. The initial FF and PCE are 82.31% and 23.34%, respectively. **i**, 3,000 h DH85 degradations of FF and power of a module. The initial FF and power are 80.2% and 331.1 W, respectively. **j**, Degradations of FF and power of a module during 600 thermal cycles between −40 °C and 85 °C. The initial FF and power are 79.5% and 331.0 W, respectively. The curves in **c** and **h**–**j** are guides to the eye, whereas the curves in **d** and **e** are fitted by normal distributions. All tests are conducted under 100 mW cm^{-2} at 25 °C.

observe that when 13 A current is applied to the cell (Fig. 4b), the FF exhibits a quite similar behaviour to that under 1 sun illumination. This implies the photon energy from light soaking is not the exclusive cause responsible for the dark conductivity increase and boron doping activation, electron-hole recombination caused by current-injected carriers probably also take effect[31].

Further increasing the light intensity from 1 to 11, 48 and 60 sun boosted the FF by $0.32 \pm 0.18\%_{abs}$, $0.39 \pm 0.14\%_{abs}$, $1.40 \pm 0.26\%_{abs}$

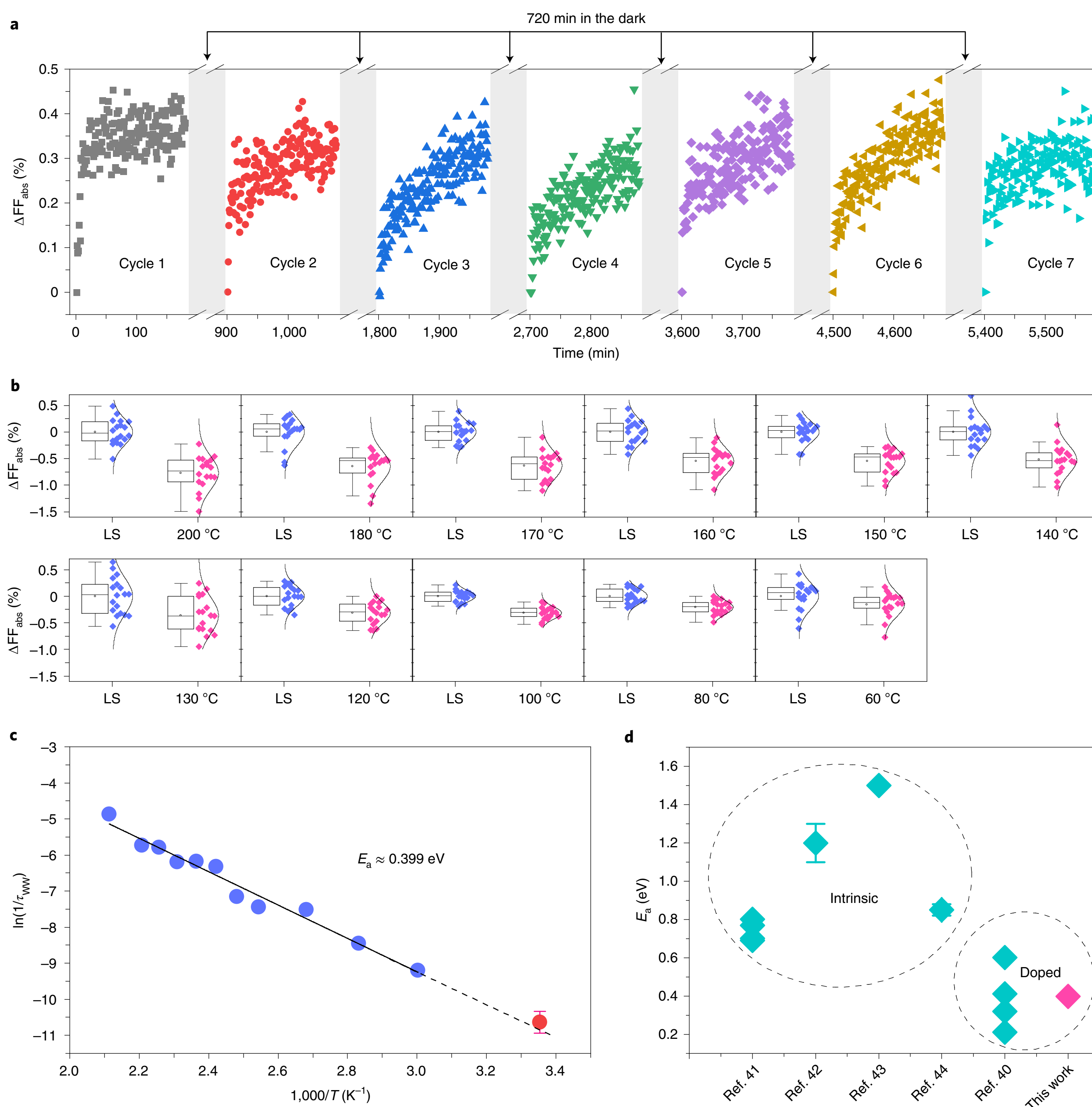

Fig. 5 | Reversible behaviour of the light-induced dark conductivity increase and boron doping activation. **a**, Evolutions of the FF (compared with the initial FF before light soaking) in alternating cycles of 180 min 1 sun illumination and 720 min sleeping in the dark. The cell size is 15.6 cm × 15.6 cm. **b**, Decay of FF in 10 min at different temperatures, the LS states are light soaked under 60 sun illumination for 70 s, followed by 25 min dark 'sleeping'. The error bars, boxes and points in the boxes are standard deviations, 25–75% distributions and mean values respectively. The curves are normal distributions. **c**, Fitting of equation (3) to the τ_{WW} (blue circles) derived from experimental average ΔFF in **b**, the red circle is picked from Supplementary Table 1 measured at 25 °C, where the error bar stems from the standard error during the fitting process of τ_{WW}. The activation energy $E_a \approx 0.399$ eV is calculated from the slope of the fitting line. Here E_a is related to the energy barrier of hydrogen movements between Si–Si bonds. **d**, Typical E_a of intrinsic and doped a-Si:H materials. The numbers along the *x*-axis are reference numbers. The error bars on mean values are standard deviations taken from refs. [42,44].

and 1.50 ± 0.37%$_{abs}$, respectively (Fig. 4c). Here the improvement in FF under 60 sun illumination is close to the ΔFF ≈ 1.8 ± 0.4%$_{abs}$ reported via a multifunctional process[36]. We also notice that increasing either the light intensity or the forward bias can improve the magnitude of ΔFF (Fig. 4c and Supplementary Fig. 8). This highlights that intensive light soaking or high forward bias activates more efficient boron doping by pumping more metastable hydrogen from B–H–Si to other configurations, in this consideration, we naturally regard SHJ solar cells as the premium choice for concentrator photovoltaic systems. At the mass-production level, 60-sun illumination obtains state-of-the-art industrial FF and PCE of 85.19 ± 0.18% and 24.46 ± 0.05%, respectively (Fig. 4d,e), together

with improved V_{oc} by ~2.6 mV (Supplementary Fig. 9), thanks to improvement of the build-in field in c-Si absorber.

Numerical investigation on these improvements is based on a traditional drift-diffusion model of the SHJ solar cell. Procedures and simulated parameters are provided in Supplementary Tables 2 and 3. Comparison of samples A and B in Supplementary Table 4 reveals the decline of N_s from 9.0×10^8 cm^{-2} to 4.3×10^8 cm^{-2} only slightly increases the FF by 0.04%$_{abs}$, much lower than the experimental 1.50 ± 0.37%$_{abs}$, but in good consistency with the PFF in Fig. 2d. Samples A and C show that the FF increases by 0.66%$_{abs}$ when the efficient doping concentration of boron (N_a) increases from 2.0×10^{18} cm^{-3} to 1.0×10^{19} cm^{-3}. Samples A and D show the FF boosts by 0.77%$_{abs}$ when the series resistance (R_s) declines from 0.4 Ω cm^2 to 0.25 Ω cm^2 (Supplementary Table 4). The collective refinements to N_s, N_a and R_s improves the FF and PCE from 83.79% and 24.0% to 85.25% and 24.5%, respectively, in good agreement with the experimental results from 83.70 ± 0.22% and 23.9 ± 0% to 85.19 ± 0.18% and 24.5 ± 0.1% (samples A and E in Supplementary Table 4). Together with that, the simulated increase of V_{oc} from 744.3 mV to 746.9 mV is also identical to the experimental results from 744.3 ± 0.7 mV to 746.9 ± 0.5 mV. Such excellent consistencies between simulations and experiments confirm the improvements in SHJ solar cells do stem from light-induced efficient doping of boron atoms.

After capping an 80 nm SiO_x antireflection layer onto a high-efficiency cell, we submitted it to an independent testing centre and achieved a certificated PCE of 25.18% with a FF of 85.42% on a 244.63 cm^2 wafer (Fig. 4f and Supplementary Fig. 10). They are among the highest certificated PCE and FF for total-area two-side contacted silicon solar cells[34] (Fig. 4g and Supplementary Fig. 11). The FF reaches 98.30% of its Shockley–Queisser limit, ~86.9% (ref. [37]). We also submitted another SHJ solar cell capped with a 110 nm MgF_2 antireflection layer to ISFH CalTeC; they reported total- (244.81 ± 0.91 cm^2) and designated-area (226.71 ± 0.91 cm^2) PCEs of 25.10 ± 0.38% and 25.45 ± 0.38%, respectively (Fig. 4f and Supplementary Fig. 12). The a bit lower FFs of 84.28% ± 0.93% and 84.63 ± 0.93% than that certificated from NPVM probably stem from the degradation between the 70 sun light soaking and the certification.

With regard to stability, FF and PCE of devices retain 98.70% and 97.59% of their initial values after 1,000 h DH85 impact (Fig. 4h), without any encapsulations. At the module level, Figs. 4i and 4j show that the FF and PCE retain 98.1% (96.8%) and 95.5% (95.4%), respectively, after 3,000 h DH85 impact (600 thermal cycles between −40 °C and 85 °C), demonstrating their high stability against extreme climate degradation factors. The DH85 (thermal-cycle) degradation of the module is threefold longer than the IEC 60068-2-78 (IEC 61215-2:2016) standard. These tests exclude the high-density (~10^{21} cm^{-3}) weakly bound hydrogen atoms in the p-a-Si:H film as the key factor that dominates the damp-heat (thermal-cycle) degradation[4].

In addition to the stabilities in DH85 and thermal cycle environments, we finally explored the reversible behaviour of SHJ solar cells caused by the light-induced dark conductivity increase and boron doping activation. As found in Fig. 5a, we alternated between measuring the cells' FFs under 1 sun illumination for 180 min and the dark for 720 min. Evidently, the FF decays ~0.3–0.35%$_{abs}$ during each sleeping in the dark. From Supplementary Fig. 13, we find that the FF rapidly declined by ~0.15%$_{abs}$ in the first ~20 min, followed by a slow decay in the next ~745 min. This fast decay time of ~20 min is consistent with the characteristic time constant $\tau_D \approx 15.84 \pm 1.55$ min of the Debye relaxation (Supplementary Table 1), confirming the enhancement of FF does stem from the improvement of conductance of doped a-Si:H film. Figure 5a also reveals that the FF rapidly climbs up after turning on the light soaking; thus, the output of power plants comprising SHJ solar cells undergoes a rapid increase after sunrise on sunny days, which challenges the present IEC testing standards, as the in-house certification underestimates their performance in real operations. The following provides a feasible pathway to freezing the dark decay. We took 198 solar cells from the same batch and divided them into 11 groups. First, the devices in each group undergo a 70 s light soaking under 60 sun illumination, followed by a 25 min sleeping in the dark to finish the fast Debye relaxation. Their FFs were then measured before and after 10 min annealing at different temperatures, as shown in Fig. 5b, the decay magnitude of FF (from Williams–Watts relaxation) dramatically drops when the temperature is decreased from 200 °C to 60 °C, which suggests that the low temperature arrests the unfavourable formation of the B−H−Si configurations. This observation agrees with the perspective that annealing can accelerate annihilation of Si−H−Si configurations[38]. Using the average ΔFF (Fig. 5b), we derived the temperature-dependent characteristic time constant τ_{WW} by the Williams–Watts model,

$$\Delta \mathrm{FF}\,(t) = \Delta \mathrm{FF}\,(0)\,\exp\left[-\left(t/\tau_{\mathrm{WW}}\right)^{\beta_{\mathrm{WW}}}\right]. \quad (2)$$

According to Kakalios and co-workers[39], the β_{WW} of a-Si:H is $0.00165T$ (in Kelvin), independent of the doping type; the τ_{WW}, on the other hand, obeys an Arrhenius relationship,

$$\ln\left(1/\tau_{\mathrm{WW}}\right) = \ln\left(1/\tau_{\mathrm{WW0}}\right) - E_a/\left(RT\right), \quad (3)$$

where R is molar gas constant. Figure 5c shows the fitting of equation (3) to the τ_{WW} (blue circles) calculated from equation (2), interestingly, the theoretical τ_{WW} (red circle) from Supplementary Table 1 is close to the extrapolation of the fitting line, confirming the validation of equation (3). The derived activation energy $E_a \approx 0.399$ eV is well agreement with the prediction of migration barrier ~0.417 eV and the 0.385 ± 0.143 eV inferred from the reported data of doped a-Si:H (ref. [40]). Figure 5d finds E_a of doped a-Si:H is noticeably smaller than that of the intrinsic counterpart[40–44], most likely owing to existence of the exclusive metastable hydrogen configurations in doped materials (as inferred from Figs. 2a and 3b). We notice phosphorus-doped a-Si:H also has smaller E_a, thus it is expected to make similar contributions to the light-induced effect. This speculation is evident from the light soaking behaviour of 'half' cells with structure of Ag/IWO/n-a-Si:H/i-a-Si:H/n-c-Si/IWO/Ag, where the p-a-Si:H is totally removed (Supplementary Fig. 14). It is interesting to find the doped a-Si:H thin films exhibit an opposite light-induced behaviour in comparison to p-type c-Si when oxygen atoms exist in the form of B_s–O_{2i} complexes inside the crystalline matrix[45]. Given doped a-Si:H has small E_a but great τ_{WW} at low temperatures, we conclude that the cold climates can effectively prevent the decay of metastable FF.

Conclusion

We observed light-soaking-induced enhancement of dark conductance of boron-doped a-Si:H thin films, which is appealing for realizing outstanding optoelectronic devices. We show that light soaking promotes the diffusion and hopping of the weakly bound hydrogen atoms, which allow the activation of $B-Si_4$ doping. The light-soaking effect noticeably improves the charge carrier transport in SHJ solar cells, yielding an excellent FF of 85.42% (84.63%) and a PCE of 25.18% (25.45%) on a 244.63 cm^2 (226.71 cm^2) total-area (designated-area) wafer.

Methods

Material characterization. Glow discharge p-a-Si:H films with thicknesses of ~60 nm were deposited onto silica glasses in 40.68 MHz very-high-frequency plasma-enhanced chemical vapour deposition (VHF-PECVD; IE Sunflower, OAK-DU-5) at 200 °C. Then 200-nm-thick 10 mm × 2 mm silver strips were thermally evaporated on the film surface to form transfer-length-method structures[46]. Current–voltage characteristics between the two strips with interval distance of 200 μm were probed by KEITHLEY 6487. This current–voltage

measurement is to qualitatively determine the existence of the light-induced changes. For FTIR (Perkin Elmer, Spectrum 100) measurements, p-a-Si:H thin films were deposited on >3,000 Ω cm float-zone c-Si substrates, their infrared absorptions from Si−H and B−H bonds were characterized using the transmission mode; H^- profiles of IWO/*i*-a-Si:H/c-Si, IWO/p-a-Si:H/c-Si and p-a-Si:H/*i*-a-Si:H/c-Si were analysed by TOF-SIMS (ION TOF, GmbH-Muenster), during which the chamber pressure, primary ion source and current are 1.0×10^{-9} mbar, 30 keV Bi^+ and 1.0 pA, respectively, the depth profiles were acquired using a 500 eV Cs^+ sputter beam. Cross-sectional images of p-a-Si:H were probed by high-resolution transmission electron microscope (FEI Titan 80-300ST), operated at 200 kV. Injection-dependent τ_{eff} and PFF were measured by the Sinton WCT-120 and Suns-Voc, respectively. The Q_s and N_s are fitted from a surface recombination model by Olibet and colleagues, they discussed details about the model and also provided the fitting codes in the appendix A of Olibet's thesis[47].

Ultrafast and broadband transient absorption spectra were measured using a homebuilt pump–probe set-up. The output of a titanium sapphire amplifier (Coherent LEGEND DUO, 4.5 mJ, 3 kHz, 100 fs) splits into three beams (2.0 mJ, 1.0 mJ and 1.5 mJ), two of which separately pump two optical parametric amplifiers (OPA; Light Conversion TOPAS Prime). TOPAS-1 provides tunable pump pulses and TOPAS-2 generates the probe pulses. A 1,300 nm pulse from TOPAS-2 is sent through a CaF_2 crystal mounted on a continuously moving stage. This generates a white-light supercontinuum pulses from 350 nm to 1,100 nm. The pump pathway length is varied between 5.12 m and 2.60 m with a broadband retroreflector mounted on an automated mechanical delay stage (Newport linear stage IMS600CCHA controlled by a Newport XPS motion controller), thereby generates delays between pump and probe from −400 ps to 8 ns. Pump and probe beams are overlapped on surface of the p-a-Si:H. By a beam viewer (Coherent, LaserCam-HR II) we regulate the size of pump beam about three times larger than the probe beam. The probe beam is guided to a custom-made prism spectrograph (Entwicklungsbüro Stresing) where it is dispersed by a prism onto a 512 pixel complementary metal–oxide semiconductor linear image sensor (Hamamatsu G11608−512DA). The probe pulse repetition rate is 3 kHz, whereas the excitation pulses are mechanically chopped to 1.5 kHz (100 fs to 8 ns delays), and the detector array is read out at 3 kHz. These characterizations are also summarized in Supplementary Table 5.

The transient absorption signals are fitted by the one-dimension recombination and diffusion model:

$$\frac{\partial N(x,t)}{\partial t} = D\frac{\partial^2 N(x,t)}{\partial x^2} - \left(k_1 N(x,t) + k_2 N^2(x,t) + k_3 N^3(x,t)\right).$$

The initial condition is $N(x,0) = N(0,0)\exp(-\alpha x)$, and the boundary condition at the front/back surface/interface are $\frac{\partial N(x,t)}{\partial x} = \frac{S_f}{D}N(0,t)$ at $x=0$ and $\frac{\partial N(x,t)}{\partial x} = -\frac{S_b}{D}N(d,t)$ at $x=d$, respectively. $N(x, t)$ is the carrier density, which is a function of the time t and the position x in the film, D is the diffusion coefficient, k_1, k_2, k_3 are the first-, second- and third-order bulk recombination constants, α is the absorption coefficient, and S_f and S_b are the front and back interface/surface recombination velocities. The front surface/interface is exposed to the pump laser beam. The general rate equation consists of the diffusion equation and includes the different recombination rates present in the bulk. $N(x, t)$ is proportional to $\Delta T/T$, $N(x,t) = \beta\frac{\Delta T}{T}$ with a fitted prefactor β.

Molecular dynamics and ab initio calculations. The simulations were conducted on the platform of Materials Studio 2017R. We used the Tersoff empirical potential to express the atomic interactions for a-Si and a-Si:H, which has been demonstrated for amorphous tetrahedral semiconductors[48]. Rectangular c-Si supercells of 10.854 Å × 10.854 Å × 21.708 Å composed of 128 silicon atoms were heated up to 3,000 K at a rate of 540 K ps^{-1} followed by 200 ps equilibrium to fully destroy small crystallinities. The metallized liquid silicon was then quenched to 300 K at a slow rate of 1.0×10^{11} K s^{-1}. The slow cooling efficiently reduces structure defects such as dangling bonds and floating bonds. Two hydrogen atoms were introduced into the silicon network, followed by relaxations at constant volume using the generalized gradient approximations of Perdew–Burke–Ernzerhof. To gain p-type doping, we replaced various tetrahedral silicon sites by one boron atom, followed by geometrical relaxations. To investigate the capture of hydrogen by boron, we placed hydrogen atoms >2.3 Å away (much longer than B−H and Si−H single bonds) from the boron atoms and relaxed to observe the coordinate changes. The functional, ensemble, temperature and simulation time are generalized gradient approximations of Perdew–Burke–Ernzerhof, NVT, 298 K and 0.3 ps, respectively. These $Si_{127}BH_3$ amorphous supercells were used as the starting points for further calculations. The reaction barriers were calculated by transition-state searches between optimized structures using the generalized synchronous transit method[49]. Each case was statistic by calculating 30 different $Si_{127}BH_3$ amorphous supercells because the fluctuations of bond length and bond angle in the amorphous network may introduce some uncertainty.

Device fabrication. Czochralski *n*-c-Si wafers were purchased from Sichuan Yongxiang Silicon Material Company. Their initial thickness and electrical resistivity are ~160 μm and 0.3−2.1 Ω cm respectively. The saw damage was etched in 20.0 vol% alkaline solution at 80 °C for 2 min, followed by formation of surface pyramids via immersion in 2.1 vol% alkali solution at 80 °C for 8 min. They then experienced standard RCA cleaning to remove surface organics and metal ions. After that, these wafers underwent 3 min dipping in 2.0% hydrofluoric acid water solution to remove the surface oxide. In the chambers of very-high-frequency plasma-enhanced chemical vapour deposition (VHF-PECVD, 40.68 MHz; Ideal Energy Sunflower), 5 nm *i*-a-Si:H, 15 nm p-a-Si:H, 4 nm *i*-a-Si:H and 6 nm *n*-a-Si:H were sequentially deposited on the two faces of the clean wafers. The process temperatures were 200 ± 10 °C. The *i*-a-Si:H layer consists of two sublayers, their power density and chamber pressure during deposition are 67/40 mW cm^{-2} and 50/80 Pa respectively. The first layer was deposited using pure SiH_4, while the second layer was deposited using diluted SiH_4 in H_2 with a ratio of $[SiH_4]:[H_2] = 1:10$. 15 s H_2 plasma was applied to treat the two *i*-a-Si:H films for improving the passivation quality at the *i*-a-Si:H/*n*-c-Si interfaces. Power density, chamber pressure and gas flow ratio during deposition of the *n*-a-Si:H were 33 mW cm^{-2}, 80 Pa and $[PH_3]:[SiH_4]:[H_2] = 1.5:100:1000$. The p-a-Si:H layer also has two sublayers, whose power density, chamber pressure and gas flow ratio during deposition were 20/20 mW·cm^{-2}, 80/80 Pa and $[B_2H_6]:[SiH_4]:[H_2] = 1:100:100/2:100:400$ respectively. About 80 nm IWO was grown on both sides of the devices by the reactive plasma deposition (RPD, DS1-12080-SN-D13; Shenzhen S.C.) at 150 °C, whose target material is 1.0% tungsten-doped in indium oxide. Nine silver busbars and fingers were screen printed on the two faces of the devices using low-temperature paste, followed by annealing at 150 °C for 5 min and 185 °C for 30 min. For the certificate cell, an 80 nm SiO_x layer was capped onto the sun-side surface in a 13.56 MHz radio-frequency PECVD (ULVAC CME-400).

Device characterization. Current–voltage characteristics of all solar cells without SiO_x antireflection were tested under standard conditions (25 °C, 100 mW cm^{-2}) using a solar simulator (Halm IV, ceitsPV-CTL2). The light intensity was calibrated using a certified National Renewable Energy Laboratory (NREL) reference cell. The submitted cell with SiO_x antireflection was independently tested by the NPVM in the Fujian Province, China, one of the designated test centres for the solar cell efficiency tables. The device area was captured by an automatic image test system. Before certification, it was light soaked for 30 min under 1 sun illumination, followed by cooling down to room temperature. The cell with MgF_2 antireflection layer was independently tested by ISFH CalTeC, which experienced a 1 sun illumination before the measurement. The conveyor during light soaking was pre-heated to ~200 °C, and the light intensity was adjusted from 1 to 60 sun (ASIA NEO TECH INDUSTRIL Company, NLIDR-S60; red light). These cells were quickly cooled down by cold-air blowing after the light soaking. All devices were measured under standard conditions. These characterizations are also summarized in Supplementary Table 6.

Damp-heat degradation. The devices underwent 1,000 h damp-heat impact at DH85 in the dark, during which they were in open-circuit condition. These devices are six-inch SHJ solar cells without any encapsulations. The 60-cell module underwent 3,000 h damp-heat impact at DH85 in the dark according to the IEC 60068-2-78, during which it was in open-circuit condition. All measurements were conducted under standard conditions (25 °C, 100 mW cm^{-2}), out of the climate test chamber.

Thermal cycle degradation. The thermal cycles were conducted in accordance with the IEC 61215-2:2016. The cycle temperature was between −40 °C and 85 °C. The applied current was 100% I_{mpp} at the rising edge of temperature.

Simulation procedures and parameters of SHJ solar cells. The rear-junction SHJ solar cell was modelled using the traditional drift-diffusion models on the AFORS-HET device-simulation platform previously developed for heterojunction solar cells[50]. General parameters are listed in Supplementary Table 2. The effects of N_s, N_a and R_s on the device performances are different. N_s represents chemical passivation, which is dominated by defect density at the a-Si:H/c-Si interfaces. Q_s represents the surface charge density at the depletion region of the p–n junction, which cannot be directly used in the simulation. As an alternative option, we use N_a to represent the field passivation. R_s represents transport series resistance in the device, here its variation mainly stems from the bulk resistance of p-a-Si:H as has been observed in Fig. 1a. Both N_a and R_s are dominated by the doping efficiency of boron in the p-a-Si:H film. N_s is derived from modelling the τ_{eff} of IWO/p-a-S i:H/*i*-a-Si:H/*n*-c-Si/*i*-a-Si:H/*n*-a-Si:H/IWO, measured before and after 70 s light soaking under 60-sun illumination. R_s was measured from the solar simulator under the standard conditions. N_a is the only optimized parameter to matching the experimental V_{oc}, J_{sc}, FF and PCE of SHJ solar cells before and after the 70 s 60-sun illumination. Samples A and E in Supplementary Tables 3 and 4 are control samples, whose performances are very close to those of the as-prepared and light-soaked (60 sun) SHJ solar cells respectively. To distinguish the effects of N_s, N_a and R_s on the performance of SHJ solar cells, samples B–D in Supplementary Tables 3 and 4 change N_s, N_a and R_s one by one. By this means, we can determine the key factors that dominate the device-level light-induced changes.

Reporting Summary. Further information on research design is available in the Nature Research Reporting Summary linked to this article.

Data availability
All data generated or analysed during this study are included in the published article, its Supplementary Information and Source Data. Source Data are provided with this paper.

Received: 17 August 2021; Accepted: 28 March 2022;
Published online: 12 May 2022

References
1. Lin, C. L., Chen, F. H., Wang, M. X., Lai, P. C. & Tseng, C. H. Gate driver based on a-Si:H thin-film transistors with two-step-bootstrapping structure for high-resolution and high-frame-rate displays. *IEEE Trans. Electron Devices* **64**, 3494–3497 (2017).
2. Lin, L. D., Xu, X. N., Chu, C. X., Majeed, M. K. & Yang, J. Mesoporous amorphous silicon: a simple synthesis of a high-rate and long-life anode material for lithium-ion batteries. *Angew. Chem. Int. Ed. Engl.* **55**, 14063–14066 (2016).
3. Shah, A., Torres, P., Tscharner, R., Wyrsch, N. & Keppner, H. Photovoltaic technology: the case for thin-film solar cells. *Science* **285**, 692–698 (1999).
4. Liu, W. et al. Damp-heat-stable, high-efficiency, industrial-size silicon heterojunction solar cells. *Joule* **4**, 913–927 (2020).
5. Yoshikawa, K. et al. Silicon heterojunction solar cell with interdigitated back contacts for a photoconversion efficiency over 26%. *Nat. Energy* **2**, 1–8 (2017).
6. Ashouri, A. A. et al. Monolithic perovskite/silicon tandem solar cell with >29% efficiency by enhanced hole extraction. *Science* **370**, 1300–1309 (2020).
7. Street, R. A. Doping and the Fermi energy in amorphous silicon. *Phys. Rev. Lett.* **49**, 1187–1190 (1982).
8. Kugler, S., Pusztai, L., Rosta, L., Chieux, P. & Bellissent, R. Structure of evaporated pure amorphous silicon: neutron-diffraction and reverse Monte Carlo investigations. *Phys. Rev. B* **48**, 7685–7688 (1993).
9. Jiang, J. et al. Electric-field-enhanced crystallization of amorphous silicon. *Nature* **395**, 481–483 (1998).
10. Sriraman, S., Agarwal, S., Aydil, E. S. & Maroudas, D. Mechanism of hydrogen-induced crystallization of amorphous silicon. *Nature* **418**, 62–65 (2002).
11. Deringer, V. L. et al. Origins of structural and electronic transitions in disordered silicon. *Nature* **589**, 59–64 (2021).
12. Cattin, J. et al. Influence of light soaking on silicon heterojunction solar cells with various architectures. *IEEE J. Photovolt.* **11**, 575–583 (2021).
13. Bao, S. et al. The rapidly reversible processes of activation and deactivation in amorphous silicon heterojunction solar cell under extensive light soaking. *J. Mater. Sci: Mater Electron.* **32**, 4045–4052 (2021).
14. Kobayashi, E. et al. Light-induced performance increase of silicon heterojunction solar cells. *Appl. Phys. Lett.* **109**, 153503 (2016).
15. Staebler, D. L. & Wronski, C. R. Reversible conductivity changes in discharge-produced amorphous Si. *Appl. Phys. Lett.* **31**, 292–294 (1977).
16. Staebler, D. L. & Wronski, C. R. Optically induced conductivity changes in discharge-produced hydrogenated amorphous silicon. *J. Appl. Phys.* **56**, 3262–3268 (1980).
17. Hamed, A. J. Persistent photoconductance in doping-modulated and compensated a-Si:H. *Phys. Rev. B* **44**, 5585–5602 (1991).
18. Stutzmann, M. Role of mechanical stress in the light-induced degradation of hydrogenated amorphous silicon. *Appl. Phys. Lett.* **47**, 21–23 (1985).
19. Shlesinger, M. F. & Montroll, E. W. On the Williams–Watts function of dielectric relaxation. *Proc. Natl Acad. Sci. USA* **81**, 1280–1283 (1984).
20. Chamberlin, R. V., Mozurkewich, G. & Orbach, R. Time decay of the remanent magnetization in spin-glasses. *Phys. Rev. Lett.* **52**, 867–870 (1984).
21. Kriza, G. & Mihály, G. Stretched-exponential dielectric relaxation in a charge-density-wave system. *Phys. Rev. Lett.* **56**, 2529–2532 (1986).
22. Coey, J. M., Ryan, D. H. & Buder, R. Kohlrausch thermal relaxation in a random magnet. *Phys. Rev. Lett.* **58**, 385–388 (1987).
23. Gezo, J. et al. Stretched exponential spin relaxation in organic superconductors. *Phys. Rev. B* **88**, 140504 (2013).
24. Bube, R. H., Echeverria, L. & Redfield, D. Evidence for a stretched-exponential description of optical defect generation in hydrogenated amorphous silicon. *Appl. Phys. Lett.* **57**, 79–80 (1990).
25. Kumar, K., Mishra, S. K., Baev, I., Martins, M. & Pandey, D. Evidence for the coexistence of spin-glass and ferrimagnetic phases in $BaFe_{12}O_{19}$ due to basal plane freezing. *Chem. Commun.* **56**, 14897–14900 (2020).
26. Pandey, A., Cai, B., Podraza, N. & Drabold, D. A. Electrical activity of boron and phosphorus in hydrogenated amorphous silicon. *Phys. Rev. Appl.* **2**, 054005 (2014).
27. Boyce, J. B. & Ready, S. E. Nuclear-magnetic-double-resonance investigation of the dopant microstructure in hydrogenated amorphous silicon. *Phys. Rev. B* **38**, 11008 (1988).
28. Fedders, P. A. & Drabold, D. A. Theory of boron doping in a-Si:H. *Phys. Rev. B* **56**, 1864 (1997).
29. Santos, P. V. & Jackson, W. B. Trap-limited hydrogen diffusion in a-Si:H. *Phys. Rev. B* **46**, 4595–4606 (1992).
30. de Walle, C. G. V. Energies of various configurations of hydrogen in silicon. *Phys. Rev. B* **49**, 4579–4585 (1994).
31. Morigaki, K. & Hikita, H. Modeling of light-induced defect creation in hydrogenated amorphous silicon. *Phys. Rev. B* **76**, 085201 (2007).
32. Darwich, R. et al. Observation by infrared transmission spectroscopy and infrared ellipsometry of a new hydrogen bond during light-soaking of a-Si:H. *Philos. Mag. B* **72**, 363–372 (1995).
33. Sinton, R. A. & Cuevas, A. A quasi-steady-state open-circuit voltage method for solar cell characterization. In *16th Eur. Photovoltaic Solar Energy Conf.* 1152–1155 (WIP-Renewable Energies, 2000).
34. Green, M. et al. Solar cell efficiency tables (version 57). *Prog. Photovolt. Res. Appl.* **29**, 3–15 (2020).
35. Lei, Y. S. et al. A fabrication process for flexible single-crystal perovskite devices. *Nature* **583**, 790–795 (2020).
36. Wright, M. et al. Multifunctional process to improve surface passivation and carrier transport in industrial n-type silicon heterojunction solar cells by 0.7% absolute. *AIP Conf. Proc.* **2147**, 110006 (2019).
37. Rühle, S. Tabulated values of the Shockley–Queisser limit for single junction solar cells. *Sol. Energy* **130**, 139–147 (2016).
38. Buda, F., Chiarotti, G. L., Car, R. & Parrinello, M. Structure of hydrogenated amorphous silicon from ab initio molecular dynamics. *Phys. Rev. B* **44**, 5908–5911 (1991).
39. Kakalios, J., Street, R. A. & Jackson, W. B. Stretched-exponential relaxation arising from dispersive diffusion of hydrogen in amorphous silicon. *Phys. Rev. Lett.* **59**, 1037–1040 (1987).
40. Street, R. A., Biegelsen, D. K. & Knights, J. C. Defect states in doped and compensated a-Si:H. *Phys. Rev. B* **24**, 969–984 (1981).
41. Wolf, S. D., Ballif, C. & Kondo, M. Kinetics of a-Si:H bulk defect and a-Si:H/c-Si interface-state reduction. *Phys. Rev. B* **85**, 113302 (2012).
42. Santos, P. V. & Jackson, W. B. Trap-limited hydrogen diffusion in a-Si:H. *Phys. Rev. B* **46**, 4595–4606 (1992).
43. Dersch, H., Stuke, J. & Beichler, J. Light-induced dangling bonds in hydrogenated amorphous silicon. *Appl. Phys. Lett.* **38**, 456–458 (1981).
44. Dersch, H., Schweitzer, L. & Stuke, J. Recombination processes in a-Si:H: spin-dependent photoconductivity. *Phys. Rev. B* **28**, 4678–4684 (1983).
45. Macdonald, D. et al. Light-induced boron-oxygen defect generation in compensated p-type Czochralski silicon. *J. Appl. Phys.* **105**, 093704 (2009).
46. Reeves, G. K. & Harrison, H. B. Obtaining the specific contact resistance from transmission line model measurements. *IEEE Electron Device Lett.* **3**, 111–113 (1982).
47. Olibet, S. et al. Properties of interfaces in amorphous/crystalline silicon heterojunctions. In *23rd International Conference on Amorphous and Nanocrystalline Semiconductors (ICANS 23)* 651–656 (Wiley, 2009).
48. Tersoff, J. Empirical interatomic potential for carbon, with applications to amorphous carbon. *Phys. Rev. Lett.* **61**, 2879–2882 (1988).
49. Govind, N., Petersen, M., Fitzgerald, G., King-Smith, D. & Andzelm, J. A generalized synchronous transit method for transition state location. *Comput. Mater. Sci.* **28**, 250–258 (2003).
50. Stangl, R., Kriegel, M. & Schmidt, M. AFORS-HET, version 2.2, a numerical computer program for simulation of heterojunction solar cells and measurements. In *IEEE 4th World Conference on Photovoltaic Energy* 1350–1353 (IEEE, 2006).

Acknowledgements
W.L. acknowledges professor Z. Ma and W. Ji for their fruitful discussions. W.L. acknowledges the financial supports from National Natural Science Foundations of China (grant no. 62004208) and Science and Technology Commission of Shanghai Municipality (grant no. 22ZR1473200). L.Z. acknowledges the financial support from National Natural Science Foundations of China (grant no. 62074153). A.H. acknowledges the financial support from Science and Technology Commission of Shanghai Municipality (grant no. 19DZ1207602).

Author contributions
W.L. conceived the idea, proposed the concept of a light-induced dark conductivity increase and boron doping activation, designed the overall experiments and led the project. J.S., L.Z., W.L., A.H., F.M., Y.X. and H.L. performed device optimization. W.L., J.Y. and J.W. performed molecular dynamics and ab initio simulations, and modelled the experimental data. W.L. performed SIMS analysis. A.H. performed current–voltage measurements under 11, 48 and 60 sun. S.H., X.L., J.P., Y.Y., K.J. and Z.M. measured the 1 sun FF evolutions. J.D. performed the RCA cleaning. Q.S. and Y.Yu performed the system calibrations of the solar simulator. Z.Li performed the FTIR measurements. H.Z. and J.S. performed the FF evolutions at different temperatures. Y.Y., K.J. and S.H. performed the Sinton measurements. Y.Y. and W.L. performed the dark current–voltage measurements. X.L. performed the damp-heat measurements. Y.Y., K.J. and X.L. performed the PFF measurements. J.L. performed the modelling of Sinton data. Z.D., J.Y., X.Y., X.S., L.X., J.K., F.X., J.L. W.Z. and S.D.W. discussed Sinton data, molecular dynamics and ab initio simulations. Y.G. and F.L. performed the transient absorption measurements and analysis. W.L. and Z.L. supervised the project. W.L. wrote the paper. All authors contributed to the discussion of the results and revision of the manuscript.

Competing interests

J.S., L.Z., A.H., J.D., H.Z., H.L., Y.X., F.M. and Z.L. are employees of Zhongwei New Energy (Chengdu) Company. H.Z., H.L., Y.X. and Z.L. are employees of Tongwei Solar Company. J.L. is an employee of UISEE Technologies (Shanghai) Company. All other authors declare no competing interests.

Additional information

Supplementary information The online version contains supplementary material available at https://doi.org/10.1038/s41560-022-01018-5.

Correspondence and requests for materials should be addressed to Wenzhu Liu or Zhengxin Liu.

Peer review information *Nature Energy* thanks Patrick Burr, Bram Hoex and Delfina Muñoz for their contribution to the peer review of this work.

Reprints and permissions information is available at www.nature.com/reprints.

Publisher's note Springer Nature remains neutral with regard to jurisdictional claims in published maps and institutional affiliations.

Open Access This article is licensed under a Creative Commons Attribution 4.0 International License, which permits use, sharing, adaptation, distribution and reproduction in any medium or format, as long as you give appropriate credit to the original author(s) and the source, provide a link to the Creative Commons license, and indicate if changes were made. The images or other third party material in this article are included in the article's Creative Commons license, unless indicated otherwise in a credit line to the material. If material is not included in the article's Creative Commons license and your intended use is not permitted by statutory regulation or exceeds the permitted use, you will need to obtain permission directly from the copyright holder. To view a copy of this license, visit http://creativecommons.org/licenses/by/4.0/.

© The Author(s) 2022

nature research

Corresponding author(s): Wenzhu Liu, Zhengxin Liu

Solar Cells Reporting Summary

Nature Research wishes to improve the reproducibility of the work that we publish. This form is intended for publication with all accepted papers reporting the characterization of photovoltaic devices and provides structure for consistency and transparency in reporting. Some list items might not apply to an individual manuscript, but all fields must be completed for clarity.

For further information on Nature Research policies, including our data availability policy, see Authors & Referees.

Experimental design

Please check: are the following details reported in the manuscript?

1. Dimensions

Item	Yes/No	Response
Area of the tested solar cells	☒ Yes ☐ No	244.63 square centimeter, 244.81 square centimeter and 226.71 square centimeter
Method used to determine the device area	☒ Yes ☐ No	Device characterization in Method.

2. Current-voltage characterization

Item	Yes/No	Response
Current density-voltage (J-V) plots in both forward and backward direction	☐ Yes ☒ No	Forward direction is enough for our silicon cells.
Voltage scan conditions *For instance: scan direction, speed, dwell times*	☒ Yes ☐ No	Forward direction from -0.1 V to 0.78 V; 100 points; integral time 5 ms; delay time 5 ms.
Test environment *For instance: characterization temperature, in air or in glove box*	☒ Yes ☐ No	Device characterization in Method.
Protocol for preconditioning of the device before its characterization	☒ Yes ☐ No	Device characterization in Method.
Stability of the J-V characteristic *Verified with time evolution of the maximum power point or with the photocurrent at maximum power point; see ref. 7 for details.*	☒ Yes ☐ No	Figures 4h, 4i, 4j; Supplementary Figure 13

3. Hysteresis or any other unusual behaviour

Item	Yes/No	Response
Description of the unusual behaviour observed during the characterization	☐ Yes ☒ No	Silicon cells do not exhibit hysteresis under standard conditions.
Related experimental data	☐ Yes ☒ No	Silicon cells do not exhibit hysteresis under standard conditions.

4. Efficiency

Item	Yes/No	Response
External quantum efficiency (EQE) or incident photons to current efficiency (IPCE)	☒ Yes ☐ No	Supplementary Figure 10
A comparison between the integrated response under the standard reference spectrum and the response measure under the simulator	☐ Yes ☒ No	Certificate reports do not contains this comparison.
For tandem solar cells, the bias illumination and bias voltage used for each subcell	☐ Yes ☒ No	They are not tandem solar cells.

5. Calibration

Item	Yes/No	Response
Light source and reference cell or sensor used for the characterization	☒ Yes ☐ No	Supplementary Figure 10
Confirmation that the reference cell was calibrated and certified	☒ Yes ☐ No	Device characterization in Method. A certified NREL reference cell. Reference cell in ISFH is unknown.

Calculation of spectral mismatch between the reference cell and the devices under test

☐ Yes
☒ No

Certificate report does not contains this mismatch comparison.

6. Mask/aperture

Size of the mask/aperture used during testing

☒ Yes
☐ No

Two are conducted as total-area testing, one is conducted as designated-area testing. The later uses an aperture mask (ISFH identifier FN018) shadowing about 3 mm of the cell edges.

Variation of the measured short-circuit current density with the mask/aperture area

☒ Yes
☐ No

From 40.04 to 40.46 mA/cm2

7. Performance certification

Identity of the independent certification laboratory that confirmed the photovoltaic performance

☒ Yes
☐ No

Supplementary Figures 10 and 12. Certified by NPVM, one of the designated test centers for solar cell efficiency tables; and ISFH CalTeC, Germany. Full reports are found as source data along with the publication.

A copy of any certificate(s)
Provide in Supplementary Information

☒ Yes
☐ No

Supplementary Figures 10 and 12; Full reports are found as source data along with the publication.

8. Statistics

Number of solar cells tested

☒ Yes
☐ No

In the main body of the paper. 316 + 198 +1 + 1 = 516 devices.

Statistical analysis of the device performance

☒ Yes
☐ No

Figures 4d, 4e, Supplementary Figure 9.

9. Long-term stability analysis

Type of analysis, bias conditions and environmental conditions
For instance: illumination type, temperature, atmosphere humidity, encapsulation method, preconditioning temperature

☒ Yes
☐ No

Damp-heat degradation and thermal cycle degradation in Method.